

# SIMULATION

<http://sim.sagepub.com/>

---

## **Simulating Passive Microwave Radiometer Designs Using Simulink**

Derek M. Burrage, Mark A. Goodberlet and Malcolm L. Heron

*SIMULATION* 2002 78: 36

DOI: 10.1177/0037549702078001201

The online version of this article can be found at:

<http://sim.sagepub.com/content/78/1/36>

---

Published by:



<http://www.sagepublications.com>

On behalf of:



Society for Modeling and Simulation International (SCS)

**Additional services and information for *SIMULATION* can be found at:**

**Email Alerts:** <http://sim.sagepub.com/cgi/alerts>

**Subscriptions:** <http://sim.sagepub.com/subscriptions>

**Reprints:** <http://www.sagepub.com/journalsReprints.nav>

**Permissions:** <http://www.sagepub.com/journalsPermissions.nav>

**Citations:** <http://sim.sagepub.com/content/78/1/36.refs.html>

# Simulating Passive Microwave Radiometer Designs Using SIMULINK

**Derek M. Burrage**<sup>1</sup>

Australian Institute of Marine Science  
Townsville M.C., 4810, Australia

**Mark A. Goodberlet**

ProSensing Inc.  
107 Sunderland Road, Amherst MA 01002

**Malcolm L. Heron**

School of Mathematical and Physical Sciences  
James Cook University, Townsville, Qld, 4811, Australia

The authors have developed a simulation system for a passive microwave radiometer using MATLAB and SIMULINK from The MathWorks, Inc. The system comprises a high-level block diagram simulation for a modern instrument, the Scanning Low Frequency Microwave Radiometer, or SLFMR. The hardware prototype SLFMR, which was designed to map sea surface salinity, was implemented using the classic pulsed noise injection Dicke radiometer design. A suite of lower-level user-written components arranged in user block libraries has also been developed. The simulations functionally model the signal flow of the prototype, with random fluctuations representing the equivalent noise temperature of various signals propagating through the system, so the fundamental physics of random noise processes are preserved. Examples of several simulations are presented, and the computational feasibility, performance, and possible enhancements are assessed.

**Keywords:** Simulation, microwave radiometer, sea surface salinity, MATLAB, SIMULINK

## 1. Introduction

Passive microwave radiometers find application in many disciplines including astronomy, earth science, meteorology, and oceanography. Our interest lies in instruments designed to observe sea surface salinity, although with minor modifications, the same instruments can be adapted for soil moisture measurement.

Early investigations of the relationship between ocean surface microwave emission and salinity by Sirounian (1968) [1] and Paris (1969) [1, 2] led to successful airborne radiometer transect measurements of the Mississippi outfall by Droppelman and Mennella [3] and Thoman [4]. Remote sensing of sea surface salinity from space was first achieved from Skylab [5], and sensitive airborne systems were flown over Chesapeake Bay by Blume et al. [6, 7]. However, the hardware technology and retrieval algorithms have only recently matured sufficiently to make precise and accurate 2-D mapping of sea surface salinity in coastal and open ocean regions a practical proposition [8]. This is timely as population development pressures and defense

priorities focus attention on the coastal zone and as salinity is increasingly seen to play a role in global ocean/atmosphere exchange processes.

In the early 1990s, the University of Massachusetts Microwave Remote Sensing Laboratory and ProSensing, Inc. (then known as Quadrant Engineering, Inc.), in collaboration with the National Aeronautics and Space Administration (NASA), Goddard Space Flight Center and the National Ocean and Atmospheric Administration (NOAA) developed and tested two new multibeam instruments for remotely mapping sea surface salinity and soil moisture. Although Electronically Scanned Thinned Array Radiometer (ESTAR) [9] was primarily developed to map soil moisture, it was used successfully by Le Vine et al. [10] to map the Delaware coastal current from a NASA P-3 aircraft. The Scanning Low Frequency Microwave Radiometer (SLFMR) [11], which is optimized for observing salinity, has been used extensively to map salinity from a DeHaviland Beaver aircraft flying over US east and south coast estuaries and coastal waters [12, 13]. Both these instruments operate as interferometers, but the beam-forming process is implemented using software in ESTAR and

**Submission Date:** November 1999

**Accepted Date:** August 2001

*SIMULATION*, Vol. 78, Issue 1, January 2002 36-55  
© 2002 The Society for Modeling and Simulation International

1. Current address: The University of Southern Mississippi, Department of Marine Science, Building 1020, Room 157, Stennis Space Center, MS 39529. E-mail: derek.burrage@usm.edu.

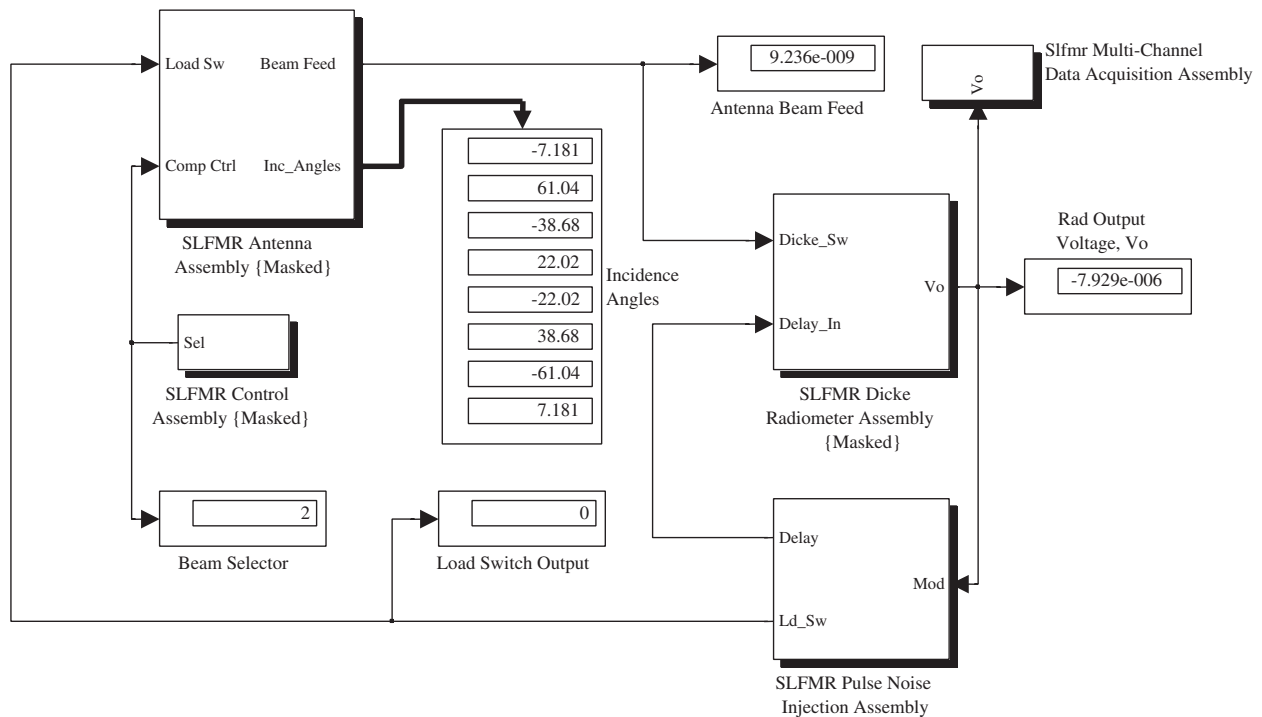


**Figure 1.** Main system block diagram for scanning low frequency microwave radiometer (SLFMR) model Sflmrx11h showing antenna, radiometer, data acquisition, and control assemblies

hardware in the SLFMR. Our present simulation work is focused on the SLFMR.

In these applications, the instrument is mounted underneath the aircraft with its dipole array mounted pointing vertically downward. A beam-forming matrix is used to synthesize eight antenna beams, which are arranged symmetrically in pairs pointing at acute angles to the nadir in the cross-track direction. The SLFMR samples the beams sequentially using a “fly back” scanning procedure [11]. The observed brightness temperatures are a function of the sea surface dielectric constant and less dominant factors such as surface roughness, while the dielectric constant is strongly influenced by conductivity and temperature. Since temperature is sensed independently using a companion infrared radiometer system, the instrument can be used to infer conductivity and hence to estimate the sea surface salinity [14].

A second SLFMR has recently been built for an Australian research consortium and a lighter and more sensitive version, known as Salinity, Temperature and Roughness Remote Sensor (STARRS), based on the principles of the Hach design [15], is being developed. Proposals have also been made for satellite-borne salinity mapping instruments [8, 16], and a variety of technologies, designs, and deployment methods are being considered for global soil moisture and salinity mapping missions.

Given these new developments, and the relatively high cost of developing hardware prototypes, especially for satellites, we decided to assess the feasibility of simulating entire new instrument designs at the signal processing level (in contrast to the electronic component level, which can

be analyzed using proprietary software, e.g., SPICE), before undertaking detailed hardware design. Our primary goal is thus to investigate the feasibility and utility of developing a simulation system that would help to reduce development time and costs, and assess alternative designs and performance before hardware is assembled. To facilitate validation, we do this for an existing instrument design and prototype. If the approach is successful, we will proceed to use it to assess new designs prior to hardware prototype construction. Developing a capability to evaluate changes to specifications and nonstandard design features, along with instrument training, is an important secondary goal.

Near real-time simulation of a radio frequency (RF) analogue instrument operating at L-band frequencies on a single CPU digital computer running at MHz clock rates is practically impossible, but we have found that by scaling the operating frequencies within design limits, useful predictions of instrument functions and performance can be made, despite the simulation running considerably slower than the hardware prototype.

## 2. Description of the Simulation System

### 2.1 Simulation Software

The simulation software used includes The MathWorks, Inc. PCWIN MATLAB version 5.3.0 with Signal Processing Toolbox V4.2, Real-Time Workshop V 3.0.0, and SIMULINK V 3.0. The C compiler was WATCOM 11.0. The models were run on an INTEL 133 MHz Pentium

**Table 1.** Model size and execution speed. Each model (col. 1) is characterized by the number of channels (2), the antenna frequency (3), number of SIMULINK blocks (4), the real-time ratio (5), and the simulation time (6). The final entry (col. 7) describes the processor used.

Run Mode/Model	Number of Channels	Antenna Frequency (kHz)	Number of Blocks	Real-Time Ratio	Simulation Time (seconds)	Processor
Interactive (running in block diagram mode, with minimal graphics)						
Slfmr12c	1	10	318	3400	0.1	AMD K6 300
Workspace (calling simulation from a script within MATLAB workspace)						
Slfmr12c	1	10	318	598	0.1	AMD K6 300
Slfmr12c	1	10	318	549	1.0	AMD K6 300
Slfmr09u	8	10	1033	2401	0.1	AMD K6 300
Slfmr09u	8	10	1033	8316	0.1	Intel P 133
Compiled (Watcom C *.exe running in W98 DOS Window from MATLAB work space)						
Slfmr12c	1	10	318	16	10.0	AMD K6 300
Slfmr12c	1	10	318	37	10.0	Intel P 133
Slfmr12h	1	10	321	16	10.0	AMD K6 300
Slfmr12h	1	10	321	39	10.0	Intel P 133
Slfmr14a	1	200	318	314	6.0	AMD K6 300
Slfmr14a	1	200	318	811	6.0	Intel P 133
Slfmr13a	1	200	318	303	6.0	AMD K6 300
Slfmr13a	1	200	318	740	6.0	Intel P 133
Slfmr09u	8	10	1033	1260	10.0	AMD K6 300
Slfmr11h	8	200	1030	2652	6.0	AMD K6 300

Laptop PC under Microsoft Windows 95 with 40 Mbyte RAM and 100 Mb virtual memory, and on an AMD K6 300 MHz Pentium Desktop PC under Windows 98 with 128 Mbyte RAM and about 4 Gb virtual memory. All models were run using the SIMULINK ode5 (Dormand Price) fixed step solver.

### 2.1.1 Model Structure

Models are constructed in SIMULINK via a readily customized interactive graphical user interface to a hierarchical block diagram structure (e.g., main diagram, Fig. 1 and nested subsystems, Figs. 3 and 4). The block diagrams provide a dynamic symbolic representation of the underlying code, which may be either interpreted or compiled. Models are constructed by dragging and interconnecting graphical components from built-in or user libraries within the work space, and they can be reused as subsystems of larger models and saved in user libraries. Two libraries were constructed for the present project (not shown): *Micro\_lib* contains simulated microwave and signal processing components (e.g., antenna beam formers, Dicke switches, filters, VFOs, etc.), while *Instr\_lib* holds test instruments such as phase and amplitude detectors, which are inserted as diagnostic probes. Instruments such as spectral and correlation analyzers are also provided in SIMULINK built-in libraries. To illustrate the benefits of this modular approach, the SLFMR radiometer simulation reported here

took several months to develop from scratch, while a second radiometer simulation, a Hach dual reference Dicke radiometer with automatic gain control [15], was constructed in a few weeks, largely using reusable software components from the SLFMR simulation. For brevity, the Hach simulation is not described here, but it showed that as the library expands, quite complex radiometer designs can be developed within a few days, much quicker than is possible with hardware prototypes. Once developed, each radiometer design becomes a template for refined or modified versions, which can be customized for particular applications.

### 2.1.2 Running Models

Models may be developed and run interactively in the Block Diagram Mode from the SIMULINK work space. In this mode, the user can modify certain parameters (but not model structure) on the fly and receive updated visual results during the run. This feature greatly facilitates testing, debugging, and tuning. Once constructed and saved in \*.mdl files, the models may also be invoked automatically inside \*.m file scripts running in the MATLAB workspace (using function "sim"). In both cases, the model code is interpreted, and models of the size and complexity reported here are too slow for repeated calibration and operational runs, though sufficiently fast for most testing and debugging. These models speed up by two orders of magnitude

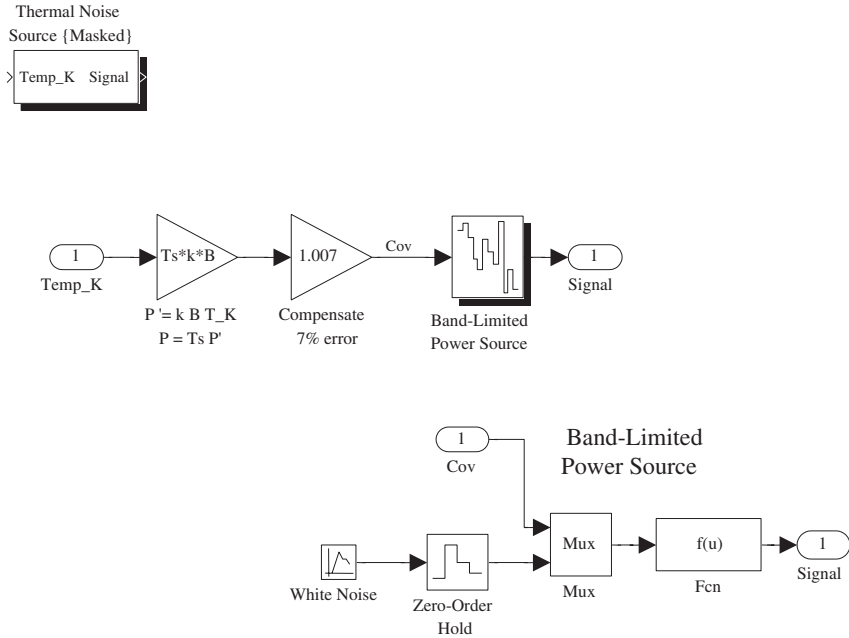


**Figure 2.** The Thermal Noise Source (top left), its block diagram (center), and the encapsulated Band-Limited Power Source block (lower right)

after automatic translation into C using the MATLAB Real-Time Workshop and compilation in the Generic Real-Time Mode using WATCOM C (Table 1).

### 2.2 Assemblies and Components

The simulation models were simply structured, with the main system block diagram comprising antenna, radiometer, and data acquisition and control “assemblies” (Fig. 1). The various “subassemblies” appear (in bold relief) at lower levels in the hierarchy (e.g., Figs. 3, 4). The antenna assembly passes antenna beam signals to the Dicke radiometer assembly where they are processed to form output voltage,  $V_o$ . This output voltage is filtered and displayed in the data acquisition assembly and is used to modulate pulses from the pulsed noise injection assembly, which are fed back to the antenna assembly to maintain balance. Beam incidence angles are also displayed. Without being comprehensive, we now illustrate how some of the generic components needed for the simulation modelling were developed and implemented. At the lowest level, these subsystems are based on built-in SIMULINK components (unbolded) or MATLAB functions. A functional description of the key SLFMR assemblies, some of the more system-specific subsystems (e.g., the Butler matrix), and the manner in which these are integrated to form a fully functional radiometer model are detailed in Section 3.

#### 2.2.1 Noise Sources

A radiometer is essentially a very sensitive calibrated radio receiver for measuring electromagnetic noise emitted by an

environmental target or scene (e.g., the atmosphere, ocean surface, or a star). This is typically achieved by comparing the target noise level (the “signal”) with the noise levels of internal and/or reference noise sources (e.g., a noise diode, antenna load, or deep space). Hence, both the signal and various instrumental noise sources (desirable or spurious) comprise random fluctuations in phase and intensity that are associated with specific power levels and equivalent noise temperatures. Here, we chose to use Gaussian probability distributions of given variance for all noise (and “signal”) sources. The noise variance represents the power  $P$  (Watts) of the noise source equivalent to a specified noise temperature  $T$ , calculated using

$$P = kTB, \tag{1}$$

where  $T$  = absolute temperature (deg K),  $B$  = source or amplifier bandwidth (Hz),  $k$  = the Boltzman constant ( $1.38 \times 10^{-23} \text{ J kg}^{-1}$ ).

This formula is derived from Planck’s blackbody radiation law via the Rayleigh-Jeans approximation [17 (pp. 186-200)].

While different noise types and probability distributions could easily be implemented, we assume all noise sources are white noise of given variance and simulate them using the MATLAB random normal number generator (“randn”). Since the model “time step” limits the possible fluctuation time scales, the white noise is bandwidth-limited (as defined by Bendat and Piersol [18 (p. 126)]).

The thermal noise source (Fig. 2, top left) is a component of the Micro\_lib signal sources subsystem. Its block

diagram (center) illustrates how the noise temperature from the masked dialog box (not shown) sets the power level in the encapsulated band-limited power source block (lower right). The latter was adapted from the SIMULINK band-limited white noise block. The thermal noise block thus accepts a specified noise temperature (deg K) as an input, converts this to an appropriate power level, or variance (“Cov” in the diagram), using equation 1, above, and outputs a corresponding fluctuating “voltage” signal. Thus, scene temperatures can be specified conventionally, while faithfully representing the underlying physics.

The dialog box associated with the masked thermal noise block allows the user to specify parameters prior to compilation or interactive execution. The parameters specified include the sample time, a random number seed, and Boltzmann constant. The sample time must be longer than the (fixed) simulation time step. In operational simulations, random number seeds were set differently for each instance of the block used in the model, and for each run, to ensure statistically independent outcomes.

### 2.2.2 Signal Processing

Some of the generic components used are simply implemented by emulating an ideal response using appropriate built-in blocks. For example, simple amplifiers and attenuators are represented by a masked built-in gain block with gain or loss factor specified in decibels. Losses in components such as switches can be similarly computed. More sophisticated amplifier blocks allow internal amplifier noise and bandwidth to be optionally specified. Pulse generators are used in several places in the instrument to trigger and synchronize switching operations. These are implemented using the built-in masked pulse generator block. The Dicke switch, usually a microwave circulator in hardware, is simply a masked subsystem comprising a clocked dual-input/single-output switch, with a gain block to specify a loss factor (typically, 0.3 dB). Circulator switching delays could also be simulated if desired. The square law detector is implemented using a product block to literally square the input signal. Again, it would be possible to implement a nonideal response, but we have chosen not to because in the SLFMR hardware the detector is close to ideal, and in the balanced Dicke design the feedback loop keeps the detector close to its linear operating point.

### 2.2.3 Filters and Integrators

Other components are more sophisticated. Analogue filters were adapted from the MATLAB version 4.2 SIMULINK filter demonstration blocks (strangely, omitted from MATLAB 5+ versions) to perform low, high, and bandpass operations using fifth-order Butterworth filters. These are implemented by masking a state-space representation of the filter with the desired response parameters calculated using the Signal Processing Toolbox. Special precautions were taken with high-order filters to account for settling times and propagation delays. Simpler single pole filters (transfer function:  $H(s)=1/(s+k)$ ) were used for less demanding audio frequency filtering. An ideal integrator ( $1/s$ )

was used in the SLFMR integrator, which functions as an integral controller. The chosen level of sophistication depends on the purpose of the simulation and is a trade-off between a desire for realism and the need to minimize computational load and settling times and avoid unnecessary complexity. If radio-frequency interference is an issue (as it was for the development of the SLFMR hardware [11], and is here), then the RF bandwidth filter design should have a sharp cutoff. If not, a lower-order filter with a gentle rolloff and faster settling time is more efficient.

## 2.3 Numerical Simulation Issues

### 2.3.1 Computational Feasibility

It is not obvious that a digital computer running at CPU clock rates of order 100 MHz could usefully simulate an analog microwave radiometer measuring fluctuations up to 100 GHz! Fortunately our application (sea surface salinity) requires antenna operation within the protected astronomical band at 1.4 GHz, which confines it to the lower (L-band) microwave range. At first glance, this might suggest we are only an order of magnitude short of the necessary “computational bandwidth” (defined as the computer clock frequency). However, in our “stochastic approach,” we simulate noise processes requiring many floating point operations (hence clock cycles) to generate each random deviate, and we must process the sequence long enough to simulate signal processing operations. This adds perhaps two orders of magnitude to the required computational bandwidth, giving about 1 MHz of useable CPU bandwidth. Unfortunately, the prototype instrument must also span a wide range of frequencies to process the incoming (L-band) signal fluctuations and provide useful information at a sample measurement interval (order 1 second) suited to the instrument platform speed and target spatial scale. The overall instrument frequency span is thus of order 1 Hz to 1 GHz, or a factor of  $10^9$ ! (By “frequency span,” we mean the range of all reception, switching, and filtering frequencies used in the instrument, in distinction to “bandwidth,” which is usually limited to a single critical component.) To simulate the required switching and signal processing operations, we must fit the simulated frequency span within a factor of  $1 \text{ MHz}/1 \text{ Hz} = 10^6$ , an impossible task, given the complexity of all but the simplest (e.g., total power) microwave radiometer designs. Fortunately, for successful simulation, we need not run the model in real time, but we could run, say, 600 times slower to recoup two or more orders of magnitude. At this rate, 1 second of instrument observing time is simulated in 10 minutes of wall clock time. This allows practical tests of instrument function and satisfactory assessment of certain performance factors. Such simulation rates are achievable even for the higher-frequency compiled models, at least for single-channel versions. At this rate, it requires 25 days to simulate an hour of survey time, so practical simulation of an entire airborne survey on a PC using this approach is still some years away.

In view of the computational challenges of the stochastic approach, an obvious and readily implemented alternative is a simulation based on analytical model equations, which are available for the SLFMR and Hach designs. This more idealized approach is fast computationally and is appropriate if developmental and computational effort are focused on simulating environmental influences, salinity retrieval algorithms, or airborne surveys. Since our present concern is solely with instrument design, we use the analytical models instead to verify the numerical simulations by indicating the ideal response. Against this standard, anomalies due to computational limitations or artifacts, specification errors, or nonideal responses can be identified.

We decided on the more computationally demanding stochastic approach to (a) discover whether microwave analogue instruments can be functionally simulated stochastically, using SIMULINK; (b) come to terms with the basic physics of the radiometer function at the signal-processing level; and (c) provide a foundation for modelling more sophisticated instruments or problems, which may not be amenable to theoretical analysis in the future, for example, instruments having unusual noise statistics, strongly nonlinear functions or responses, and cross-coupling among components.

### 2.3.2 Accuracy and Sensitivity

By accuracy, we mean the proximity of temperature measurements estimated using the simulation model to the input scene temperatures, over long time scales. Practically speaking, this is an indicator of long-term instrument drift and/or systematic biases in calibration. By sensitivity, we mean the radiometric resolution of the instrument (noise equivalent delta temperature or NEDT in radiometer parlance, henceforth  $\Delta T$ ). This is an indication of the ability of the instrument to distinguish small instantaneous changes in scene temperature in the presence of (other) noise sources, and low (high)  $\Delta T$  is synonymous with high (low) sensitivity.

We have two interpretations of accuracy and sensitivity in the present context. One, which is essentially qualitative, relates to how faithfully the simulation model functionally represents the structure and characteristic responses of the prototype, including its sensitivity to design or manufacturing quality variations. This is best considered in the context of model validation discussed below. The other concerns the ability of the simulation model, once validated and calibrated, to quantitatively predict the accuracy and sensitivity of the prototype (allowing for frequency scaling and other parameter differences). This critical issue is closely related to that of computational feasibility. By compressing the “frequency span” of the prototype to fit within the available computational bandwidth, we are reducing the statistical reliability of any simulation estimates of the accuracy and sensitivity of the prototype. To produce statistically reliable temperature estimates from the model, we must increase calibration and observing times to “dwell” longer on particular target scene temperatures, or repeat the experimental runs many times and

average the results. Even this impinges on model validation, because as simulation frequency span is reduced, the reliability with which the accuracy and sensitivity of the simulation model itself can be estimated (leaving aside the prototype) is correspondingly reduced, and this will widen confidence limits in any comparisons with analytical model parameters.

### 2.3.3 Model Development and Validation

In developing the SLFMR simulation model, the basic instrument design was extracted from published descriptions, theory, and technical specifications, and refined based on the second author’s experience in constructing the preexisting hardware prototype. This design was used to specify the required simulation model structure, function, and performance. Simulation parameters were chosen as a trade-off between programming complexity, degree of realism, and computational feasibility. Various ways of scaling the operating frequencies and switching rates were considered. Since a simple linear compression of the frequency span would waste valuable computational bandwidth, efforts were made to space the various frequencies as closely as possible, while avoiding interference between processes that should run at distinctly different rates (Table 2).

Once a basic simulation model was conceptualized, individual blocks, subsystems, and assemblies were constructed, tested, and debugged in a modular fashion then embedded in the evolving SIMULINK block diagram. Filter and integrator designs were similarly developed with desired responses. Diagnostic software instruments were constructed and added to Instr\_lib, as needed. The initial effort focused on the basic radiometer subassembly (Fig. 3). The functions performed by this assembly include amplification, predetector band pass filtering, square law detection, and a high-pass filtering to block DC signals. The Dicke radiometer assembly (Fig. 4) was built around this. Its functions include antenna/reference switching at the Dicke clock rate, synchronous detection via the analogue switch, low-pass filtering, and integration. The variable transport delay ensures synchronous demodulation by compensating for finite signal propagation delays between the Dicke and analog switches.

The pulsed noise injection assembly (Fig. 5) was constructed to close the feedback loop. The output voltage,  $V_o$ , entering via Inport 1 (right), provides the modulating signal, labeled “Mod,” for the voltage controlled oscillator (center right). The resulting frequency-modulated pulses, set to a constant width by the pulse stretcher, are used to clock the load switch (top left). This switches the attenuated noise source (lower right) alternatively between a termination and Output 2 (top left), to provide a stream of noise pulses to the antenna assembly. The filter delay compensator (top right) provides the time delay for the analog switch (Fig. 4) via Output 1.

Finally, the eight-channel beam-forming (Butler) matrix was developed, and arrangements were made to multiplex the beams within the antenna assembly (Fig. 6). The eight

**Table 2.** Key Scanning Low Frequency Microwave Radiometer (SLFMR) model and prototype parameters. Columns 3, 4, and 5 show the values of parameters (col. 1) for representative low- and high-frequency models and the hardware prototype, respectively.

Parameter	Symbol	Slfmr09u <sup>†</sup> / Slfmr12c	Slfmr11h / Slfmr13a	SLFMR	Unit
Antenna frequency	$f_a$	$10 \times 10^3$	$200 \times 10^3$	$1.413 \times 10^9$	Hz
Noise injection center frequency	$f_c$	625	3125	$17.0 \times 10^3$	Hz
Injection half bandwidth	$f_{hb}$	435	2175	$17.0 \times 10^3$	Hz
Minimum pulse injection frequency		190	950	0.0	Hz
Maximum pulse injection frequency		1060	5300	$35.0 \times 10^3$	Hz
Dicke switch frequency	$f_s$	20.0	35.0	50.0	Hz
Band pass filter bandwidth	$B$	$2.0 \times 10^3$	$12.5 \times 10^3$	$26.0 \times 10^6$	Hz
DC block (hi-pass) cutoff frequency	$f_{cd}$	2.0	2.0	31.25 <sup>a</sup>	Hz
Integrator low pass cutoff	$f_{cp}(b)$	20/5	35.0	5	Hz
Dipole noise source sample time		$1.0 \times 10^{-5}$	$5.0 \times 10^{-7}$	N.A.	sec
Model fixed time step		$5.0 \times 10^{-6}$	$2.5 \times 10^{-7}$	N.A.	sec
Maximum modulation voltage	$V_{o,max}$	$2.0 \times 10^4$ / $1.0 \times 10^4$	$5.0 \times 10^4$ / $1.0 \times 10^4$	10	V
Pulse frequency conversion ratio		0.044	0.218	$3.5 \times 10^3$	Hz/V
Maximum pulse duty cycle (# pulses)		84.8 (26)	84.8 (75)	0.70 (350)	%
Minimum pulse duty cycle (# pulses)		15.2 (4)	15.2 (13)	0.00 (0)	%
Pulse width	$t_p$	$8.0 \times 10^{-4}$	$1.6 \times 10^{-4}$	$2 \times 10^{-5}$	sec
Measurement integration time <sup>†</sup>	$\tau$	1.0/0.376	0.5/0.1	0.5	sec
Dwell period (multichannel only)	$t_d$	0.5	0.5	0.5	sec
Receiver + Antenna noise temperature	$T_{REC}$	0	0	345 + 355	K
Reference temperature	$T_{ref}$	316.5	316.5	316.5	K
Noise source temperature	$T_N$	183,500	183,500	460,000	K
Noise attenuation	$L$	6.5/6.0	5.0	10.0	dB
Theoretical sensitivity <sup>†</sup>	$\Delta T$	14.2/23.3	8.0	0.57	K
Nominal loop gain	$G_L$	234/241	241/221	133.0	dB

NOTE: N.A. = not applicable.

<sup>a</sup>Determined by the time constant of an RC high-pass filter with  $R = 160 \text{ k}\Omega$ ,  $C = 0.1 \text{ }\mu\text{F}$ .<sup>†</sup>Assumes loop response time is shorter than the data acquisition averaging time (cf. Table 3).<sup>‡</sup>Slfmr12c and Slfmr13a are single-channel versions of Slfmr09u and Slfmr11h, respectively.

dipole antenna signals (center, left) feed directly into the beam-forming (Butler) matrix. The beam signals then pass to the 20-dB directional couplers, where they are combined with the pulsed noise fed back from the load switch via Inport 1 (lower center). The load switch and coupler outputs are selected in beam sequence by the control assembly via Inport 2 (labeled “Comp Ctrl”), and passed to the Dicke switch via Output 1 (center right, “Beam Feed”).

Upon completion, overall model function was evaluated against the prototype characteristics, and design misconceptions and performance anomalies were identified and resolved. During tests, simulation and design parameters were tuned to ensure sampling and switching requirements were met, and computational speed was optimized to yield practical run times. While the eight-channel SLFMR was implemented initially, it was temporarily downgraded to a one-channel version to speed up all but the final tests. For computational efficiency, the models were also implemented initially with relatively low frequencies (i.e., a small frequency span, Table 2). Once the design was

verified, higher-frequency versions with better sensitivity but longer run times were developed.

At this stage, the simulation models were thoroughly tested functionally and considered to be qualitatively accurate representations of the prototype. Various versions were calibrated and validated by comparison with analytical equations (theory) and test data (Table 3). Statistical experiments were then performed to assess model accuracy and sensitivity, and selected component specifications were varied to check robustness to variations in component specifications.

### 3. Scanning Low-Frequency Microwave Radiometer Simulation

We chose to develop an SLFMR simulation model first because fairly comprehensive design literature [11] and a fully developed and field-tested hardware prototype (the original SLFMR) were available for reference. Having validated our approach, we will then apply it to simulate the

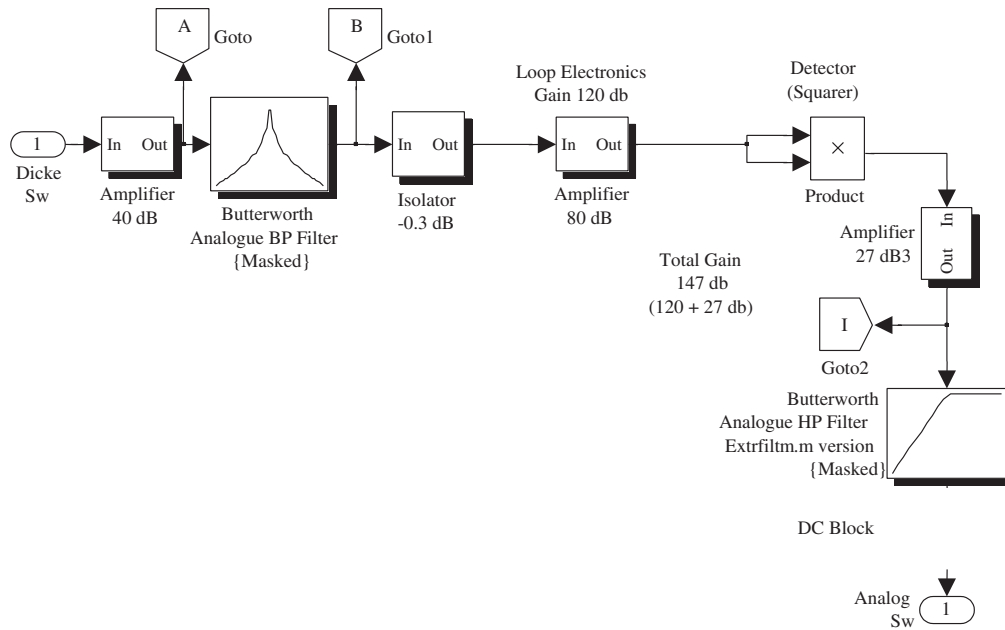


**Figure 3.** Scanning Low Frequency Microwave Radiometer (SLFMR) Sub-Assembly. This is embedded in the Dicke Radiometer Assembly (Fig. 4).

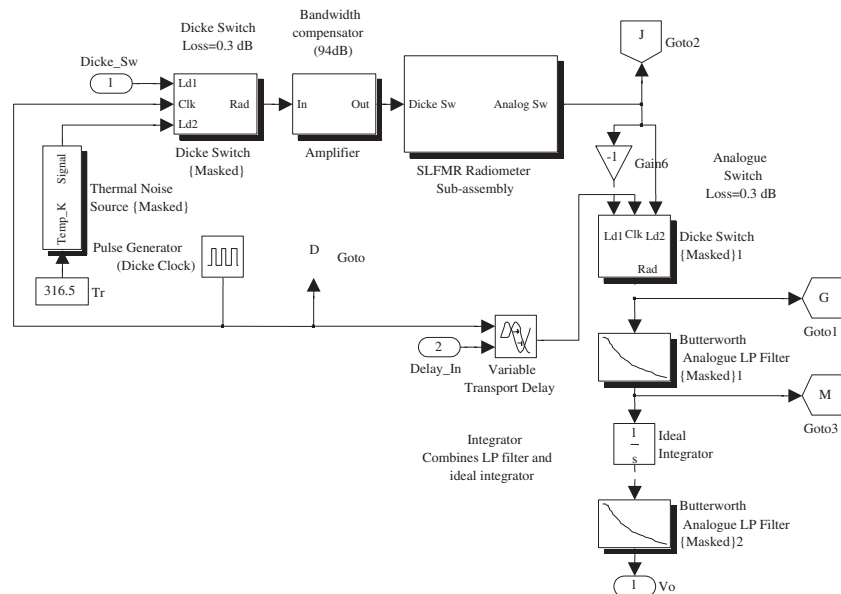


**Figure 4.** Dicke Radiometer Sub-Assembly. This is a subsystem of the main block diagram (Fig. 1), which embeds the Scanning Low Frequency Microwave Radiometer (SLFMR) Sub-Assembly (Fig. 3).

classic Hach radiometer design and its adaptation to the new STARRS design, to be described elsewhere.

### 3.1 Model Description

Only the key features of the SLFMR design are given here, since the principles of operation are well described in the literature [17]. This is a classic pulsed noise-injection

Dicke radiometer, variations of which are described by Goodberlet and Swift [11], Skou [19], and Hardy et al. [20]. This type of radiometer is immunized against the effects of RF receiver noise by switching between the antenna signal line and a reference noise source using the Dicke switch. An additional pulsed noise signal fed back into the antenna signal pathway between the beam-forming

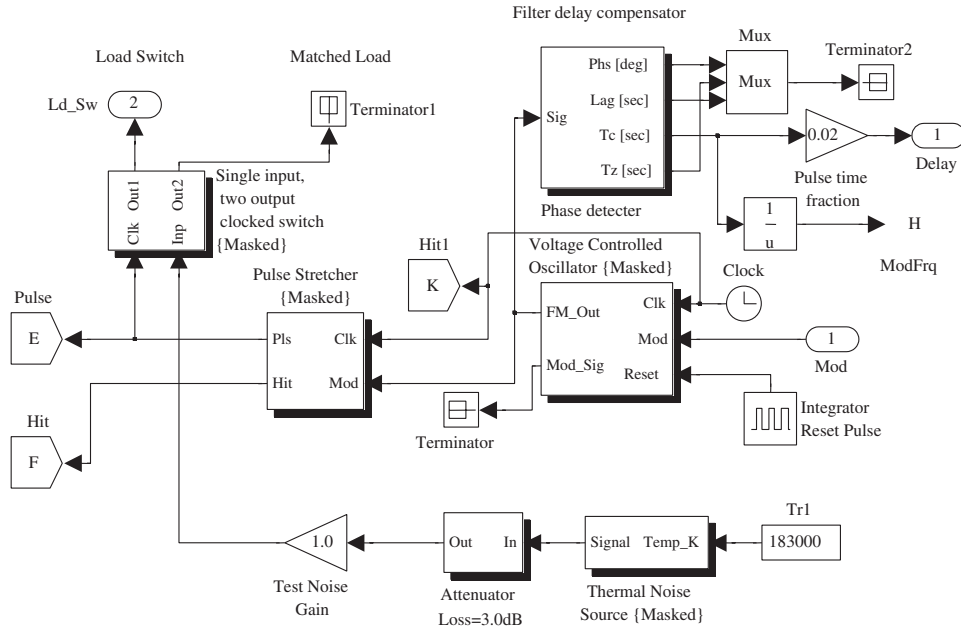


**Figure 5.** Pulsed Noise Injection Assembly. This provides feedback between the Dicke radiometer output,  $V_o$  (Fig. 4), and the antenna assembly (Fig. 6).

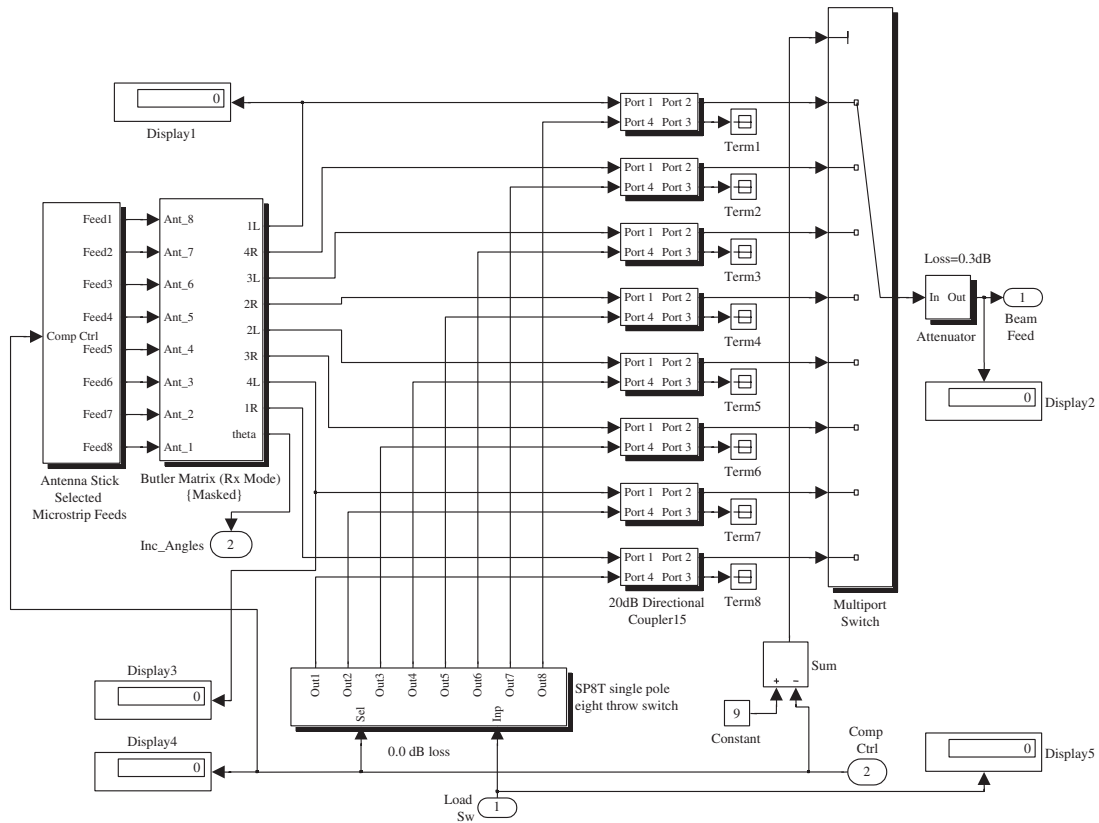


**Figure 6.** Multichannel Scanning Low Frequency Microwave Radiometer (SLFMR) Antenna Assembly. This provides eight dipole antenna signals to the beam-forming (Butler) matrix.

**Table 3.** Theoretical and model calibration and sensitivity. Models (col. 1) were calibrated as shown in italics to determine the calibration slope and offset (4, 5) and sensitivity (7), which may be compared with the corresponding theoretical values (2, 3, and 6, respectively).

Cal/Model	Theoretical Slope <sup>a</sup>	Theoretical Offset <sup>b</sup> (K)	Model Slope <sup>a</sup>	Model Offset <sup>b</sup> (K)	Theoretical <sup>†</sup> $\Delta T$ (K)	Model <sup>‡</sup> $\Delta T$ (K)	Step <sup>§</sup> Response / Int Time (sec)
Calibration A. 10 points, 3 replicates/point, $T_{sim} = 10$ sec, $V_o = a(T_a + b)$ , $R^2 = 0.9824$ :							
Slfmr12c	-61.887	-87.535	-63.969	-136.19	18.1	59.7	0.62/0.38
Calibration B. 9 points, with no replication, $T_{sim} = 100$ sec $V_o = a(T_a + b)$ , $R^2 = 0.9998$ :							
Slfmr12c	-61.887	-87.535	-62.363	-135.74	18.1	59.0	0.62/0.38
Calibration C. 2 points, 5 replicates/point, $T_{sim} = 10$ sec $V_o = a(T_a + b)$ , $R^2 = 0.9987$ :							
Slfmr12h	-131.11	-119.47	-138.84	-138.96	13.0	12.3	1.18/0.10
Calibration D. 6 points, 1 with no replication, $T_{sim} = 10$ sec $V_o = a(T_a + b)$ , $R^2 = 0.9995$ :							
Slfmr12g	-0.0928	-87.535	-0.0940	-112.68	4.7	4.3	9.2/0.10
Calibration E. 3 points, 3 replicates/point, $T_{sim} = 4$ sec $V_o = a(T_a + b)$ , $R^2 = 0.9996$ :							
Slfmr13a	-49.159	-27.426	-77.435	-156.94	6.5	6.2	0.76/0.10
Calibration F. 3 points, 5 replicates/point, $T_{sim} = 4$ sec $V_o = a(T_a + b)$ , $R^2 = 0.9993$ :							
Slfmr14a	-245.80	-27.426	-396.89	-156.53	11.1	15.1	0.26/0.10
Calibration F. 3 points, 3 replicates/point, $T_{sim} = 4$ sec $V_o = a(T_a + b)$ , $R^2 = 0.9985$ :							
Slfmr09u	-131.11	-119.47	-137.45	-136.80	13.0	10.4	1.18/1.00
Calibration F. 3 points, 3 replicates/point, $T_{sim} = 4$ sec $V_o = a(T_a + b)$ , $R^2 = 0.9997$ :							
Slfmr11h	-245.80	-27.426	-390.40	-155.89	8.0	9.1	0.26/0.50

<sup>a</sup>Slope, Offset correspond to  $a$ ,  $b$ , where  $V_o = a(T_a' + b)$ ,  $T_a'$  = input antenna temperature,  $V_o$  is output indication (Iout) following Ulaby [17 (Table 6.4)]. His eq. 6.87 along with the relationship  $f_R = (f_{hb}/V_{o_{max}}) V_o + f_c$  (see Table 2 for values) determines the linear dependence of  $V_o$  on  $T_a'$ .

<sup>†</sup> $\Delta T$  is sensitivity from Ulaby [17 (Table 6.4 & eq. 6.83)], but using empirically estimated  $e^2$ -folding step response time or averaging time  $1/(2b)$ , whichever is greater, for  $\tau$  in the bandwidth time product.

<sup>‡</sup>Found as average standard deviation of  $V_o$  for given calibration run.

<sup>§</sup>Step  $e^2$ -folding response time is time for response to be within  $(1 - 1/e^2)$  of final value in a 100- to 200-K step averaged over five model runs. The quantity after "r" is the model measurement integration time.

Butler matrix and the Dicke switch via a directional coupler bank ensures that, on average, the reference signal balances the antenna signal (including injected noise). This eliminates RF amplifier gain fluctuations and nonlinearities, while prior shifts in the relative level of the signal and noise are preserved in the integrated output signal  $V_o$ . The latter signal simultaneously modulates the noise injection levels and (once calibrated) indicates the observed antenna temperature.

To illustrate how the model was implemented, key assemblies and subsystems of the SLFMR simulation model are now described, with an emphasis on those that are unique to this design.

### 3.2 Implementation

#### 3.2.1 Antenna Assembly

This assembly (Fig. 6) simulates the signal emanating from a dipole or, for the multichannel instruments, from a dipole array coupled with a beam-forming matrix. The dipole sig-

nals are generated using the simulated thermal noise source block (described in 2.2.1). The eight-channel SLFMR antenna assembly is moderately complex. It must generate the equivalent noise power of the eight dipole antenna temperatures, carry out the beam-forming operations of the Butler matrix, and combine the injected noise with the antenna signal through the 20 dB directional couplers. In addition, the multiplexer (or multipoint switch) is provided to sequentially select the eight beams. The overall structure, as in the other assemblies, closely follows the original hardware schematics [11]. The implementation of the Butler matrix follows the diagram given in Skolnik [21 (Fig. 8.28 and pp. 311-14)], with its directional couplers and fixed phase shifters with appropriate multiples of 22.5 deg in alternate network branches.

The matrix is constructed from an array of 3-dB coupler and fixed phase delay subsystems (Fig. 7). It effectively functions as an interferometer using the 3-dB couplers and delays to transform signals from the antenna domain to the

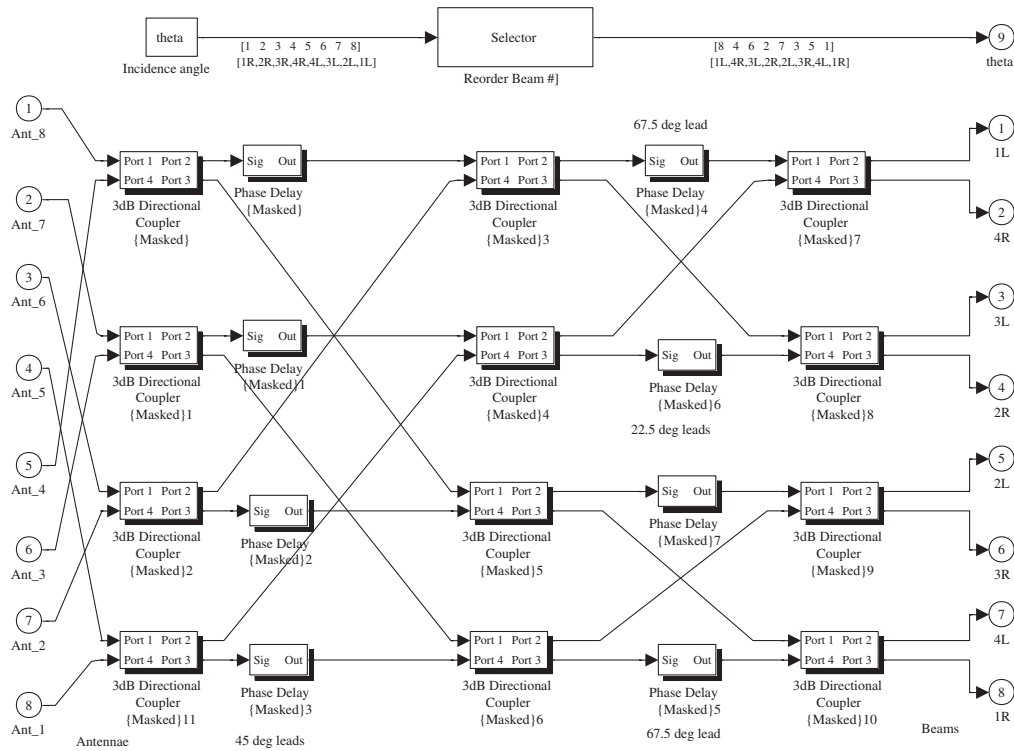


Figure 7. Block diagram for the Butler beam-forming matrix

beam domain. The antennas (Inputs 1-8, left) are numbered in reverse order of their physical location. The resulting left (L) and right (R) beams (Outports 1-8, right) are numbered (but not ordered) consecutively from the nadir direction outward. The incidence angle function (top left) uses the phase delays to compute the beam incidence angles for half wavelength dipole spacing.

The fixed phase delay employs a single masked phase delay block to introduce a transport delay time appropriate to the desired phase shift angle and nominal signal frequency (the antenna frequency), while the couplers use two such blocks in the crossover branches for each port to generate 90-deg phase shifts of appropriate sign, with gain blocks for equal power division.

### 3.2.2 Dicke Radiometer Assembly

The SLFMR Dicke radiometer assembly (Fig. 4) is of the Dicke type [22, 17] in which reference noise sources are periodically switched into the radiometer input stream to dramatically reduce the effects of RF amplifier drift in the hardware. The embedded SLFMR radiometer subassembly (Fig. 3) with its bandpass amplifier and detector resembles the sensor head of a simple total power radiometer.

### 3.2.3 Pulsed Noise Injection Assembly

The input to this assembly (Fig. 5) is the output ( $V_o$ ) from the Dicke radiometer assembly (Fig. 4). This provides feedback to eliminate the effects of RF amplifier gain variations. The feedback is provided via a system that injects noise pulses of specified level into the antenna signal line

with a variable pulse duty cycle controlled by  $V_o$ . The pulsed noise injection assembly comprises the attenuated thermal noise source, which is switched to the antenna by the load switch. The switch rate is regulated by the pulse train emitted by the Pulse Stretcher at a frequency determined by the variable frequency oscillator (VFO), modulated by  $V_o$  through input port 1. A phase detector subsystem is included to yield a finite time delay for the analog switch relative to the Dicke switch to allow for filter propagation delays. These can be neglected in the hardware prototype due to its higher operating frequencies. The filter delay compensator comprises a phase detector from Instr\_lib, which provides the zero crossing period of the modulated pulse signal and generates the analog switch time delay, as a fixed fraction of the pulse duration. The VFO generates an FM-modulated sine wave signal using a mathematical method [23], which involves integrating the modulation signal and scaling it for the desired frequency range. This quantity is used to vary the phase of a cosine signal about its center frequency. The pulse stretcher uses a zero hit crossing detector block to produce short pulses that enable a clock signal at a rate determined by the VFO output frequency. Once enabled, this clock signal, coupled with a relational operator block, extends each pulse to the preset width, so that a stream of fixed width pulses is produced at a variable rate determined by the VFO.

### 3.2.4 Data Acquisition Assembly

This assembly (shown in part in Fig. 8) performs various data processing and display, filing, power level detection,

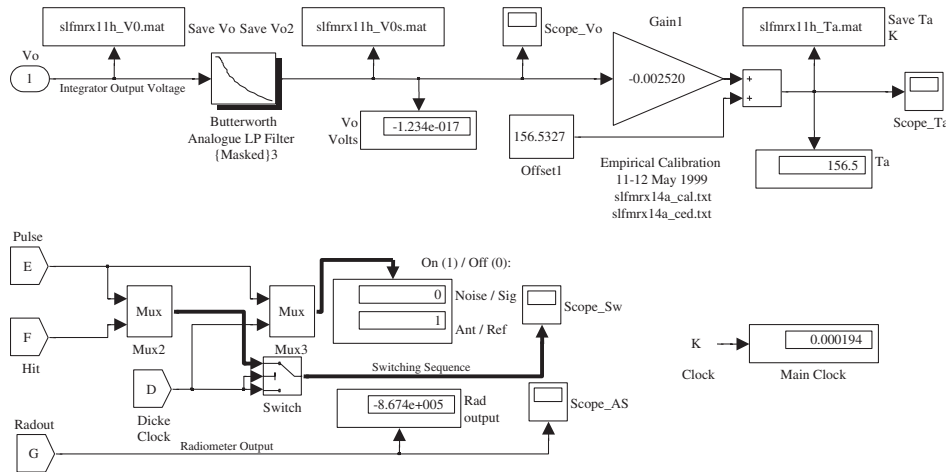


Figure 8. Data acquisition assembly

and diagnostic functions. It carries out simple signal pre-conditioning and filtering operations on the indicated output,  $V_o$ , to improve display presentation. It also applies calibration coefficients and a linear calibration equation to estimate the antenna temperature,  $T_a$  (top) from  $V_o$ . The Dicke and load switch pulses obtained via tags E and F (at left) from the pulsed noise injection assembly are also displayed (center). Finally, the analog switch output is displayed via tag G, embedded in the Dicke radiometer.

Since the assembly provides a simple set of graphical outputs (scopes and displays) accessible through a single graphical user interface window, it can also be used to provide additional diagnostic displays (not shown) from other points in the radiometer processing chain. These scopes, which tap into specific signal lines (via SIMULINK “Goto” and “From” tags) can be optionally activated during interactive runs, at the cost of slower processing, but are inaccessible during compiled runs, since MATLAB graphical functions are not provided in compiled (C-code) models. Some of these limitations are alleviated by the newly introduced C Graphics library and the Windows Real Time Target (The MathWorks, Inc.), but these would necessitate undesirable compromises in our present approach.

In the hardware prototype, the data acquisition system is implemented as a digital system that includes a multichannel analog to digital converter, together with digital processing functions, that rapidly samples the resulting discrete  $V_o$  values and averages them over successive 0.5-sec intervals. In the simulation model, data acquisition is implemented in analog form and  $V_o$  is instead smoothed using a low-pass filter of equivalent response time. We use the term *measurement integration time* in the appropriate context to denote either the averaging or equivalent smoothing time constants. Demultiplexing of the sequential eight-beam signal/data stream is achieved in software with the prototype and is not yet implemented in the model.

### 3.2.5 Control Assembly

The control assembly block (not shown) is only needed in the multichannel versions, which scan eight channels sequentially and multiplex the data through a single radiometer assembly. It is implemented using a simple three-bit (0-7) counter subsystem to provide a repeating sequence of beam numbers 1-8 at a clock interval (beam dwell time) that is preset in a mask dialog box. The antenna assembly uses this interval to multiplex the beams through the Dicke radiometer assembly.

### 3.3 Model Performance

In theory, our ready access to a hardware prototype for the SLFMR design would suggest that the simulation model could be fully verified. However, the necessity to scale the antenna and switching frequencies (Table 2), and computational limitations, prevent the simulation model from fully replicating the hardware operation and performance. The best we can achieve under these constraints is an evaluation of model performance consistent with the effects of frequency scaling and sampling restrictions.

#### 3.3.1 Calibration

The SLFMR simulation model was calibrated by doing repeated runs for various values of the input antenna temperature,  $T_a$ . Simple linear regression of  $V_o$  versus  $T_a$  was used to check linearity and determine model calibration slopes and offsets. The latter were compared with theoretical calibration slopes and offsets computed following Ulaby et al. [17 (eq. 6.87, Table 6.4, pp. 394-5)] and the linear relationship between the pulse injection frequency,  $f_R$  and  $V_o$ :  $f_R = (F_{hB} / V_{o_{max}}) V_o + f_c$ .

Results of calibrations for Sflmrx12c are shown in Figure 9. Calibration A (—+) was a nine-point calibration from 100-sec runs with no replicates. The asterisks (\*) indicate

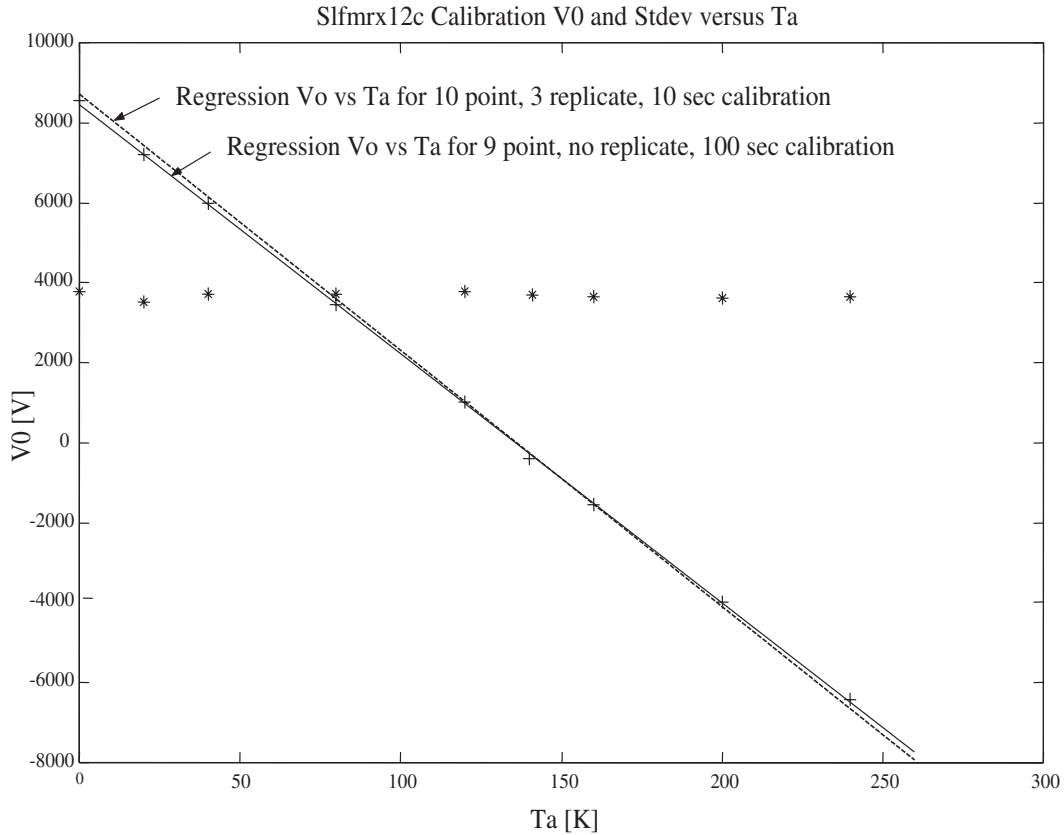


Figure 9. Regression plots of  $V_0$  versus  $T_a$  for calibration of model Slfmrx12c

corresponding standard deviations for  $V_0$  from which instrument sensitivity,  $\Delta T$ , is empirically estimated. The results for calibration B (—), a 10-point 10-sec calibration with three replicates per point (shown overlaid) were almost identical (Table 3 shows the corresponding regression parameters).

In the regression, the values of  $V_0$  used were means determined for each run (at constant  $T_a$ ), making allowance for the initial settling time by omitting the first few simulated seconds, depending on model response time, and sensitivity (see Table 3). Model linearity (as indicated by the regression  $R^2$  values in the model  $V_0$  versus  $T_a$  relationship) was found to be excellent in all models calibrated using three or more calibration points, and repeat calibrations with different numbers of points and replicates produced consistent results.

The comparison demonstrates that comparable results can be obtained using either a large number of shorter runs (A) or a smaller number of longer runs (B). Calibration coefficients, once determined, were implemented in the data acquisition subassembly so the model could subsequently display and output estimated  $T_a$  values directly.

### 3.3.2 Accuracy and Sensitivity

The model calibration and sensitivity results are compared with theoretical values in Table 3. The model sensitivity

values were estimated from the average of the standard deviations of  $V_0$  for each calibration point (or run) in a given calibration (marked by asterisks in Fig. 9 for calibration B). These generally agree closely with the  $\Delta T$  values computed from the theoretical relationship [17, (p. 379, eq. 6.83)]:

$$\Delta T = 2(T_{ref} + T_{REC}) / \sqrt{B\tau} \quad (2)$$

[17, (p. 379), Eqn 6.83],

where  $\tau$  = response time (sec),  $B$  = source or amplifier bandwidth (Hz), and  $T_{ref}$ ,  $T_{REC}$  = reference and receiver noise temperature, respectively (deg C).

Here we draw a distinction between the measurement integration time,  $\tau$ , which specifies the degree of smoothing or averaging of the indicated output voltage  $V_0$ , and the time constant of the ideal integrator/low-pass filter combination in the Dicke radiometer (Fig. 4), which partly influences the feedback loop response time. The quantity  $\tau$  is set equal to the loop response time unless the indicated output,  $V_0$  (Fig. 4), is further smoothed or averaged by the data acquisition system. Thus, if the data acquisition averaging time (time constant of the analogue LP filter, Fig. 8) is longer than the loop response time, the averaging time is used in place of the loop response time to set  $\tau$  (Table 3, col. 8).

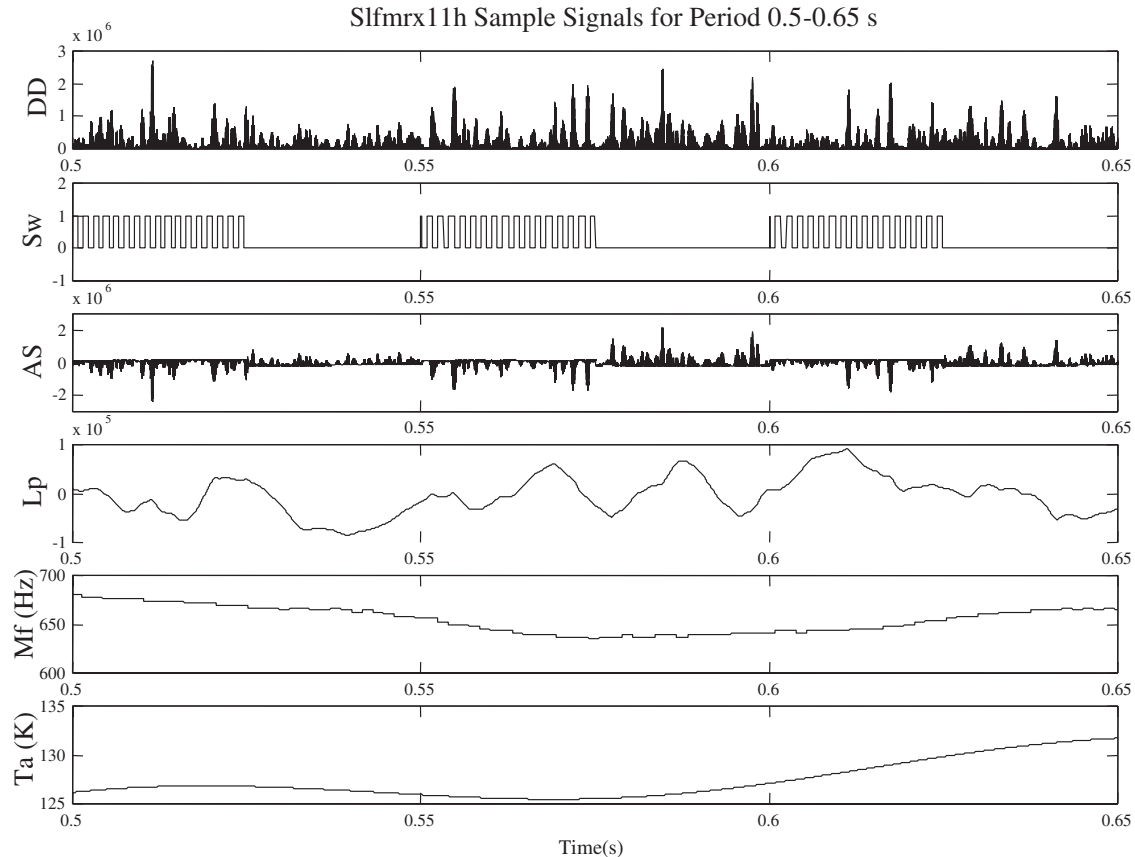


Figure 10. Sample signals for model Sifmrx11h for a 0.15-second period

In most of the simulations, we set  $T_{REC} = 0$  to minimize  $\Delta T$  and reduce the run times required to obtain statistically reliable results. However, tests conducted by injecting noise corresponding to  $T_{REC} = 345$  K using a thermal noise source placed immediately after the Dicke switch confirmed that the calibration was unchanged (due to noise cancellation resulting from the alternating sign of the analog switch output) and that  $T_{ref}$  increased in proportion to  $T_{REC}$ , as predicted by the equation above. We also injected noise into the line between the antenna output and the 20-dB coupler to simulate the effects of antenna feed and Butler matrix losses, which are estimated to total 1.8 dB (giving a loss factor of 1.514) in the hardware prototype. Unlike receiver noise, this also affects the calibration. It can be shown (Goodberlet, unpublished notes) that the  $\Delta T$  is increased in proportion to the loss factor, so the right-hand side of the above equation must be multiplied by this factor to account for the losses. Tests showed that changes in the loss factor resulted in corresponding changes to the  $\Delta T$  of the model, as predicted by the modified equation.

The empirically determined sensitivities appear better than, or comparable to, the theoretical values for all models except Sifmrx12c, which is noticeably less sensitive than theory would suggest. Also, the theoretical calibration

coefficients depart significantly from theory in several cases, for reasons we have not satisfactorily explained. However, we note that prototype hardware calibrations are normally determined empirically because they are difficult to predict reliably from theory, being highly dependent upon actual filter characteristics, and so on. The discrepancies are larger for the slower-running higher-frequency models, perhaps because the shorter simulation times used produce less reliable calibrations (unless correspondingly more replicates are used).

### 3.3.3 Execution Speed

As an inverse measure of execution speed, we used the “real-time ratio” (Table 1, col. 5), which is effectively a model “slowdown factor” relative to real time. Defined as the wall clock runtime (not shown) divided by the simulated runtime (col. 6), this ratio was found to be strongly related to processor type and model dynamics (frequency span and number of channels) and only weakly related to the number of system and library blocks (determined objectively using the SIMULINK debugger function `sldebug/list`). It was unrelated to the number of state variables (determined from the size of the state variable output vector), which was the same, 27, for all models except Sifmrx11h, which had 26. Use of data acquisition graphics

(scope blocks) slowed interactive models by factors of about 5. Compilation increased speed by about two orders of magnitude. Compiled models ran 2.5 times faster on the AMD K6 300 than the Pentium 133. For single-channel models, the higher-frequency model was slower by a factor of 13 (for the eight-channel models this factor was only 2). Compared with these, the eight-channel models (with 3 times the number of blocks), were slower by factors of 8 and 74 for the high- and low-frequency models, respectively.

The fastest model, a lower-frequency single-channel version (Slfmx12c,h), ran 16 times slower than real-time on the AMD 300 to simulate 10 seconds of observing time in under 3 minutes of wall clock time. The multichannel version (Slfmx09u) required 3.5 hours for this task! In comparison, the higher-frequency versions would require 50 minutes for the single-channel model (Slfmx13a) and 7.5 hours for its multichannel cousin (Slfmx11h).

### 3.3.4 Signal Processing

Representative signals from model Slfmx11h over a 0.05-second period illustrate the effects of the main signal processing operations (Fig. 10a-f, respectively, from top to bottom panel). Signal *DD*, output by the square law detector (Fig. 10a and tag I, Fig. 3), shows detected noise power derived alternately from the antenna assembly (including injected noise pulses) and from the temperature reference (*Tr*) provided by the thermal noise source in the Dicke radiometer assembly (Fig. 4). The signal, *Sw* (Fig. 10b, see also Fig. 8 and tags E, F, Fig. 5), the Dicke and pulsed noise switching sequence, shows three corresponding 0.05-second Dicke switch cycles, with the load switch providing rapid noise pulses that are observed in the first half of each cycle (and ignored in the second half). *AS*, the output from the analog switch (Fig. 10c, and Fig. 4, tag G), shows both the effect of the *DC* block (high-pass filter, Fig. 3), which removes the *DC* offset from *DD*, and the switch itself (Fig. 4), which inverts *DD* when it derives from the antenna assembly. The following low-pass filter (Fig. 4, tag M) is included to simulate the low-pass response of the hardware prototype analog switch. It smoothes the noise pulses and analog switch transitions to produce signal *Lp*, the low-pass filter output (d). In this model, the filter has a cutoff period of 5.7 ms (cutoff frequency of 87.5 Hz).

The integrator, which comprises an ideal integrator and 14.3 ms cutoff period ( $f_p = 35$  Hz) low-pass filter, tracks biases in the level of *Lp* (positive or negative) to form *Vo*. The effect of these operations is to make *Vo* linearly proportional to the difference  $T_{ref} - \bar{T}_a$ , where  $\bar{T}_a$  is the average of the antenna and injected noise temperatures. As well as providing an output indication, *Vo* is fed into the noise injection assembly (Fig. 5), where it sets the VFO modulation frequency, *Mf* (Fig. 10e) and hence the noise pulse duty cycle. If the radiometer becomes unbalanced,  $T_{ref} \neq \bar{T}_a$ , an excessively high or low *Vo* correspondingly increases or decreases the noise injection pulse rate, *Mf*, to compensate. Once balanced, the *Vo* level indicates how

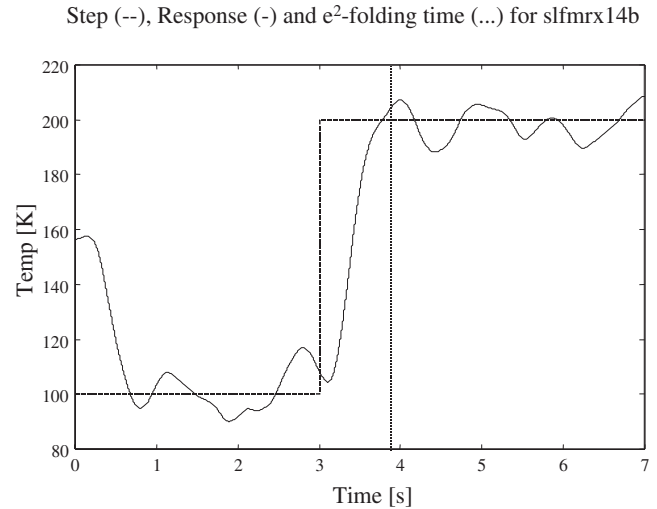


**Figure 11.** Response (–) of model Slfmx14b to 100 to 200 K brightness temperature step (– –)

much noise is being added or alternatively how low the estimated antenna temperature, *Ta* (Fig. 10f), is (excluding injected noise), relative to reference temperature, *Tref*. After further smoothing by a 0.5-second cutoff period low-pass filter (cutoff frequency 1 Hz) in the data acquisition assembly (Fig. 8), linear calibration corrections are then applied to estimate *Ta* from *Vo*.

### 3.3.5 Step Response

Model step response was estimated by forcing the models with a 100 to 200 K antenna temperature step, and averaging the resulting response times over repeated runs (Table 3, col. 8). The step response time was defined as the time required, starting from the actual step transition, for the estimated *Ta* to attain a fraction  $(1 - 1/e^2)$  or 86.5% of the 100 K step change. This time varies statistically from run to run due to variability of the *Ta* signal and associated uncertainties in instrument response, depending on instrument sensitivity. Step output from model Slfmx14b, which is identical to Slfmx14a, but with the measurement integration time increased from 0.1 to 0.5 seconds to improve sensitivity, is shown in Figure 11. The vertical line (..) marks the  $e^2$ -folding time used as an indication of the step response time (see Table 3). The model “settles” in response to the initial  $T = 100$  K temperature within 1 second of startup, and also responds to the 200 K step input at a time of 3 seconds within 1 second. The actual  $e^2$ -folding step response time for this run was estimated objectively to be 0.88 seconds. In general, the step response is determined by either the loop response time or the measurement integration time (as in this case), whichever is the greater.

### 3.3.6 Sample Output

Sample runs for various temperature time series for single-channel model Slfmx14b are shown in Figure 12a-f,

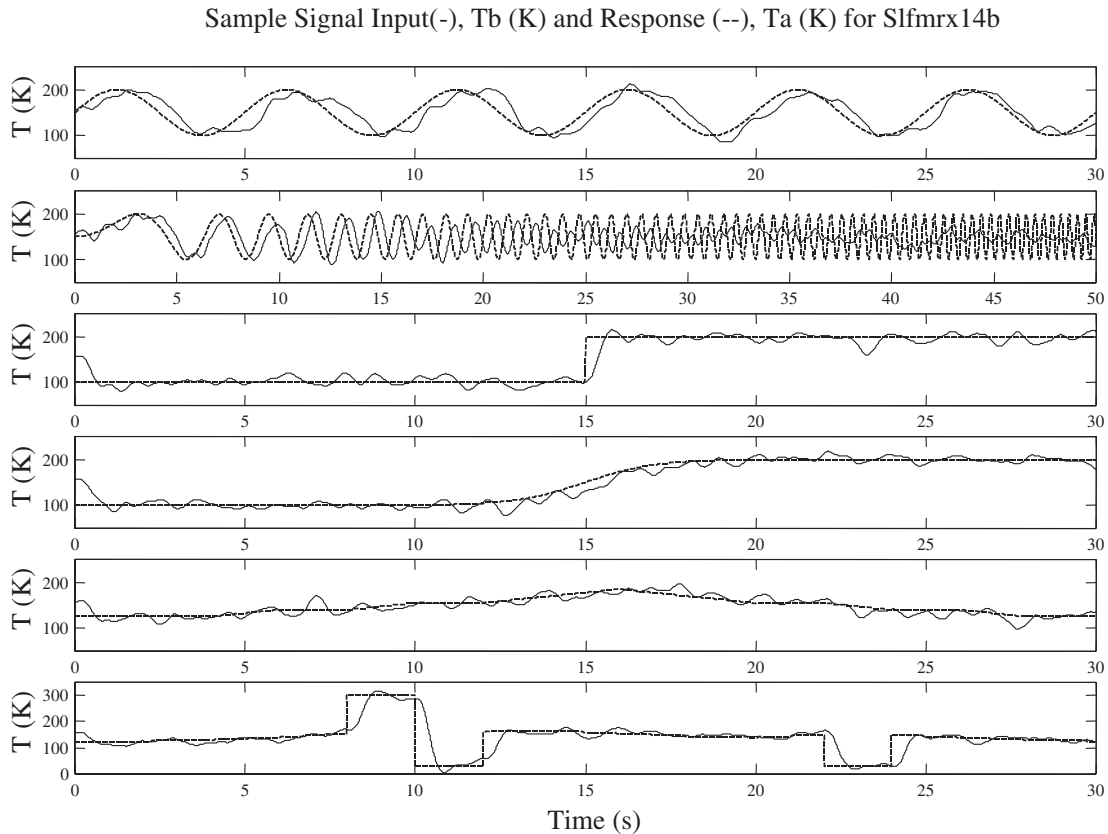


**Figure 12.** Sample outputs from 30-second model runs of Slfmr14b

with the input,  $T_b$ , overlain by the model estimate,  $T_a$ . Each subplot shows the brightness temperature input,  $T_b$  (—) and estimated antenna temperature output,  $T_a$  (---), with an initial settling time of order 1 second and an uncompensated output delay of order 0.5 second.

For a pure sine wave of amplitude 50 K and frequency 0.2 Hz or period 5 seconds (Fig. 12a, top panel), the response is sinusoidal with a delay of order 0.5 second and with random error fluctuations, corresponding to the theoretical model  $\Delta T = 8$  K, superimposed. This corresponds to a signal-to-noise ratio,  $S/N$ , of 6.3 or 8 dB. The same  $S/N$  would apply to the prototype SLFMR with  $\Delta T = 0.19$  for a sine signal amplitude of 1.2 K (i.e., for comparable  $S/N$ , a temperature change of 100 K on the plot axes could be interpreted as a 2.4 K change applied to the prototype). For a chirped sine wave (b) of amplitude 50 K with a linear input frequency diminishing from 0.001 to 1.5 Hz over 30 seconds (note extended time scale for this panel), the model response damped the signal significantly after 15 seconds when the input period was 1.3 seconds. After 20 seconds when the input period is 1.00 seconds, the response is strongly damped. It is also nearly out of phase with the input, consistent with a constant 0.5-second signal propagation delay. If the time series is extended beyond 30 seconds (to 50 seconds as shown) and correspondingly

higher input frequencies, the subsequent output resembles band limited white noise similar in power level to the output between 25 and 30 seconds, but with most of the signal filtered out. Such rapidly fluctuating sinusoidal brightness temperature patterns are unlikely to be observed in practice. An exception would be radio frequency interference due to an L-band carrier with significant modulation at (low or subaudio) frequencies that are lower than the integrator cutoff frequency.

The response to a 100 to 200 K step input (Fig. 12c, similar to Fig. 11), which shows only moderate overshoot, can be compared with the relatively smooth response to a 100 to 200 K hyperbolic tangent step  $T_b$  function (Fig. 12d). The latter could represent the brightness temperature pattern of an idealized ocean temperature or salinity front. The more gentle hill-shaped signal (e) may be taken as an arbitrary brightness temperature structure. A similar hill-shaped structure (f) is shown below this with simulated “warm” (300 K) and “cold” (30 K) calibration pulses interrupting the observations at 8–12 seconds. A subsequent cold pulse at 22–24 seconds shows that separating the warm and cold calibrations could reduce overshoot, with the observed temperature lying between these extremes. In general, the instrument response was quite accurate, with only modest overshoot for large and rapid

changes. The observed departures of  $T_a$  from the assigned  $T_b$  sequence reflect the inherent variability of the corresponding random power fluctuations, short-term model errors that are a function of sensitivity and presumably systematic biases due to calibration uncertainties.

#### 4. Discussion

We believe we have achieved our primary goal of demonstrating the feasibility and utility of developing a simulation system to help reduce the development time and costs of assessing microwave radiometer instrument designs. We adopted the more computationally demanding approach of simulating the basic instrument physics, but utilized the available analytical models to validate the model and to assess and quantify its performance. We have thus shown that the statistical properties of analog instrument designs can be investigated satisfactorily using a digital computer simulation and The MathWorks, Inc., SIMULINK system. The resulting simulation approach allows changes to instrument specifications and design features to be made simply and quickly. It also offers enough flexibility to help assess new variations of classical designs, as well as future nonstandard designs.

SIMULINK proved to be an especially flexible and efficient modelling system, which performed reliably and facilitated rapid model development and testing. It also allowed the development of custom user libraries and efficient reuse of models within a subsystem structure. The only significant limitation encountered for our purposes was the absence of analog filter designs in version 5, which necessitated the adoption and conversion of suitable demonstration subsystems from version 4. This doubtless reflects the growing emphasis on digital instrumentation, but it will be some time before we can dispense with analog electronics for the radio frequency components of microwave instruments.

The prototype SLFMR is an efficient and effective design of moderate complexity, which can be easily modelled both analytically and numerically, but a variety of other microwave radiometer designs are extant and possible (e.g., the Hach design). The simulation approach we have adopted readily lends itself to the exploration of the relative performance of such designs, including those that are less amenable to theoretical analysis. The approach also facilitates the introduction of nonstandard features and the testing of model sensitivity to variations in component specifications, which might adversely affect performance. For example, in the present model, the implications of departures from specifications of the directional couplers used in the Butler matrix can easily be tested. While the SLFMR pulsed noise injection radiometer design is essentially linear in its response, there is a number of components whose performance is, or could become, decidedly nonlinear (e.g., the square law detector). Our approach allows such effects to be simply incorporated into the model.

A number of variants of the prototype SLFMR design were simulated including both single- and multichannel versions, with various combinations of signal-processing

parameters. Two classes of model were developed with different frequency spans. This allowed rapid simulation and testing at coarse temporal and radiometric resolution, and slower simulation at fine resolution to provide more sensitive performance tests. Within each class, several models were developed with varying parameterization and calibration characteristics.

The models were validated and verified by comparing key performance criteria such as noise equivalent temperature differences,  $\Delta T$ , and step response times,  $\tau$ , with analytical models, taking into account the frequency scaling used to fit the models into the available computational bandwidth. We have summarized this information in Table 4, which also includes comments on the characteristics and application of each of the models tested. The data used to compile this table were derived from Tables 1-3. The models differed mainly in response time and bandwidth, but have also been tuned, by varying other model parameters, such as loop gains (not shown) to achieve stable and reliable calibration within an acceptable dynamic range. To provide a more general framework for comparing and contrasting the models, we have represented the various quantities in nondimensional form, by dividing by the corresponding theoretical (Table 4, col. 4) or hardware prototype (Table 4, cols. 5-7) characteristics. Thus, column 4 of Table 4 is  $\Delta T$  of the model divided by theoretical value, and column 5 is  $\Delta T$  for the model divided by that for the prototype. This allows for easy intercomparison of models and could be used in a general way to evaluate a variety of microwave radiometer models against theoretical or prototype performance.

Comparing the various coarse resolution models, S1fmr12g has the smallest  $\Delta T$  relative to the prototype (Table 4, col. 5), but this is obtained at the expense of a longer integration time. This model is unsuitable for applications with fast platform speed or rapid temporal variations in target characteristics. A hardware version of this model could be attached to a jetty or other structure to precisely monitor relatively subtle and slowly varying sea surface salinity changes. Model S1fmr12h achieves much faster response times, with decreased sensitivity. This model type could be mounted on a moving platform, such as a ship or aircraft, to sense larger variations in brightness temperature. Both this model and S1fmr13a perform closest to their theoretical  $\Delta T$  values (Table 4, col. 4; ideally,  $\Delta T$  Model/ $\Delta T$  Theory = 1). In contrast, S1fmr12c with an even faster response time, suffers from an excessive  $\Delta T$  value, due presumably to poor parameterization. We emphasize that the model response times are measured in simulation time units, not wall clock time. The wall clock response time is longer than the model response time by a factor corresponding to the real-time ratio, RTR (col. 1). Thus, model S1fmr12h, when run on the AMD K6, takes  $16 \times 2.4 \times 0.5 = 19$  seconds or 0.32 minutes of wall clock time to respond to a step input, given the prototype step response time of 0.5 second.

The multichannel model, S1fmr09u, offers both acceptable sensitivity and short step response times and has the

**Table 4.** Comparison of model characteristics. Models (col. 1) of one or eight channels (2) are shown with real-time ratio for the AMD K6 processor using compiled C code (3). The model sensitivity,  $\Delta T$  is divided by the corresponding theoretical (4) and prototype value (5). The step response time,  $\tau$  (6), and sensitivity time product, (7), are similarly normalized.

Run Mode/Model	Number of Channels	RTR AMD K6 Compiled <sup>a</sup>	$\Delta T$ Model/ Theor	$\Delta T$ Model/ Proto	$\tau$ Model/ Proto	$\Delta T \sqrt{\tau}$ Model/ Proto	Comments
Coarse resolution models—Antenna frequency model/prototype: $7.1 \times 10^{-6}$ ; Bandwidth model/prototype: $7.7 \times 10^{-5}$							
Slfmr12c	1	16	3.3	105	1.2	117	Initial single-channel model with poor sensitivity due to marginal stability and/or poor loop gain parameterization.
Slfmr12g	1	—	0.92	8	18	32	Long integration time and higher sensitivity. Suits fixed or slowly moving platforms with slowly varying target.
Slfmr12h	1	16	0.95	22	2.4	33	Short integration time and modest sensitivity suited to faster moving platforms or more rapidly varying targets.
Slfmr09u	8	1260	0.8	18	2.4	28	Low-frequency multichannel model for mapping purposes.
Fine resolution models—Antenna frequency model/prototype: $1.4 \times 10^{-4}$ ; Bandwidth model/prototype: $4.8 \times 10^{-4}$							
Slfmr13a	1	303	0.95	11	1.5	13	Best compromise model giving good sensitivity at the expense of a longer integration time relative to prototype.
Slfmr14a	1	314	1.4	27	0.52	19	Fast response time at the expense of poorer sensitivity, associated with increased sensitivity response time product.
Slfmr11h	8	2652	1.1	16	1	16	High-frequency multichannel model for mapping purposes.

<sup>a</sup>Real-time ratio for AMD K6 processor using models compiled in C.

lowest sensitivity response time product,  $\Delta T \sqrt{\tau}$  (Table 4, col. 7). This product expresses the trade-off between the two parameters, given the nominal RF bandwidth,  $B$  (see eq. 2). Thus, given  $B$ ,  $\Delta T$  could be halved in theory, if  $\tau$  was quadrupled. Apart from the much larger RTR (it runs about 80 times slower than S1fmx12h, see Table 4, col. 1), there is no apparent degradation in performance of the multichannel model (indeed, it performs better overall than the single-channel models because of subtle differences in parameterization, which we do not dwell on here). This arises because the integration time,  $\tau$ , represents the time spent observing each antenna beam, regardless of the number of beams, which, in the multichannel version of the SLFMR, are observed sequentially. However, if the time,  $n\tau$ , required to observe all channels (antenna beams) of an  $n$ -channel system were instead spent observing one of the  $n$  targets with a single-channel system,  $\Delta T$  would improve by a factor of  $1/\sqrt{n}$  for the single-channel case. Herein lies the advantage of a true multichannel system that would avoid the time slicing inherent in the multiplexed design of the SLFMR by observing all beams simultaneously with separate microwave receivers, thus improving sensitivity.

Among the fine resolution models, S1fmx13a offers the best compromise with the lowest  $\Delta T \sqrt{\tau}$  product and lowest  $\Delta T$  relative to the prototype. S1fmx14a has a faster response time but is significantly less sensitive. The multichannel version S1fmx11h offers good all around performance and runs only about 8 times slower than the single-channel versions. Thus, the overhead for the multichannel mode of operation is less significant for the fine than for the coarse resolution models.

## 5. Conclusions

We have developed a comprehensive system for simulating passive microwave radiometer designs for environmental remote sensing. The approach demonstrates that the function and performance of an analog radiometer can be simulated using a stochastic approach in which brightness temperatures are represented by random numbers of variance corresponding to the equivalent noise power. It is made computationally tractable by compressing the span of the various operating frequencies of the instrument and allowing for this compression when evaluating simulated instrument performance against design requirements or a hardware prototype.

Our experience proved SIMULINK to be a powerful and flexible simulation environment that allows close interaction and dynamic visualization during the development process, and fast computation and execution in batch mode as the design matures. As computational speed improves, the model frequency span can be increased to improve the statistical reliability and sensitivity of the simulations. Truly comprehensive testing and real-time simulation must await speed increases of several orders of magnitude, quite a few years away for single processor PCs. Although it is useful heuristically to simulate existing instruments (in this case, the SLFMR), the approach will be of most value for

assessing the implications of new instrument designs (e.g., STARRS). For such purposes, it could be sufficient to intercompare the relative performance of alternative radiometer models and assess them against expected behavior or, when available, theoretical predictions.

Once appropriate user component libraries are created, model development and initial testing of simulation models is demonstrably faster than development of an initial hardware prototype. The slower run times of the simulation model compared with the hardware prototype is an issue during final testing, particularly for the higher-frequency and multichannel models. However, this is offset by the time required to modify and set up hardware for testing, and the comparative flexibility of software modifications. Furthermore, parallel computation (e.g., making simultaneous runs using unique random number seeds on different CPUs) would allow significant speedups, especially during final calibration, and sensitivity testing, which demands many independent runs with minor input parameter differences. Stochastic simulation is unlikely to replace hardware prototyping in the foreseeable future. Rather, we see it as a useful, economical, and complementary adjunct to more traditional hardware design and development approaches. It also seems to hold promise in investigating and optimizing unconventional instrument design features.

In the present work, we investigated the feasibility of our approach by applying it to a well-established design and an existing hardware prototype. This offered the best opportunity for testing the validity of the simulation model. In the future, we will use this approach to help develop and evaluate a new radiometer system design, for which a prototype has not yet been constructed. Simulations will then be used to assess possible changes to the design and their impact on overall system performance and ease of operation.

The new STARRS design will relegate many of the measurement processes to postprocessing software, in contrast to the SLFMR, which is a null balanced design using feedback implemented in analog hardware. The simulation model in this case will focus on front-end RF performance. While the SLFMR is a multichannel antenna system multiplexed into a single-channel receiver, the new design will be a true multichannel receiver based on Hach radiometer principles. As such, it could be more demanding computationally than the existing model. Future effort will thus be directed at alternative ways to accelerate the simulation process during the evaluation of STARRS. As techniques and computational power are advanced, the approach could perhaps be adapted to the design of more sophisticated active radars, such as altimeters and scatterometers.

## 6. Acknowledgments

The authors wish to acknowledge the support of the Australian Institute of Marine Science, ProSensing Inc., and James Cook University. Calvin Swift of the Microwave Remote Sensing Laboratory, University of Massachusetts at Amherst, is thanked for hosting visits by the first author,

and for many stimulating discussions on aspects of radiometer theory and design relevant to the SLFMR simulation work.

## 7. References

- [1] Sirounian, V. 1968. Effect of temperature, angle of observation, salinity, and thin ice on microwave emission of water. *Journal of Geophysics Research* 73:4481-6.
- [2] Paris, J. F. 1969. Microwave radiometry and its applications to marine meteorology and oceanography. Texas A&M Project 286-13 (Ref. 69-1T), pp. 120-9.
- [3] Drophleman, J. D., and R. A. Mennella. 1970. An airborne measurement of the salinity variations of the Mississippi River outflow. *Journal of Geophysical Research* 75 (30): 5909-13.
- [4] Thomann, G. C. 1973. Remote measurement of salinity in an estuarine environment. *Remote Sensing of Environment* 2:249-59.
- [5] Lerner, R. M., and J. P. Hollinger. 1977. Analysis of 1.4 Ghz radiometric measurements from Skylab. *Remote Sensing of Environment* 6:251-69.
- [6] Blume, H.-J.C., B. M. Kendall, and J. C. Fedors. 1978. Measurement of ocean temperature and salinity via microwave radiometry. *Boundary-Layer Meteorol* 13:295-308.
- [7] Blume, H.-J.C., and B. M. Kendall. 1982. Passive microwave measurements of temperature and salinity in coastal zones. *IEEE Transactions Geoscience Remote Sensing* GE-20 (3): 394-404.
- [8] Lagerloef, G.S.E., C. T. Swift, and D. M. Le Vine. 1995. Sea surface salinity: The next remote sensing challenge. *Oceanography* 8:44-50.
- [9] Le Vine, D. M., A. Griffis, C. T. Swift, and T. J. Jackson. 1994. ESTAR: A synthetic aperture microwave radiometer for remote sensing applications. *Proceedings of the IEEE* 82 (12): 1787-98.
- [10] Le Vine, D. M., M. Kao, R. W. Garvine, and T. Sanders. 1998. Remote sensing of ocean salinity: Results from the Delaware coastal current experiment. *Journal of Atmospheric and Oceanic Technology* 15:1478-84.
- [11] Goodberlet, M. A., and C. T. Swift. 1993. *A remote sensing system for measuring estuarine and coastal ocean surface salinity*. Progress Report #2 prepared for NOAA under contract 50-DKNA-1-00119 to U.S. Dept. of Commerce. p. 111. Hadley, MA: Quadrant Engineering.
- [12] Goodberlet, M. A., C. T. Swift, K. P. Kiley, J. L. Miller, and J. B. Zaitzeff. 1977. Microwave remote sensing of coastal zone salinity. *Journal of Coastal Research* 13 (2): 363-72.
- [13] Miller, J. L., M. A. Goodberlet, and J. B. Zaitzeff. 1998. Remote sensing of salinity in the coastal zone. *EOS, Transactions of the American Geophysical Union* 79 (14): 3.
- [14] Klein, L. A., and C. T. Swift. 1977. An improved model for the dielectric constant of sea water at microwave frequencies. *IEEE Journal of Oceanic Engineering* OE-2 (1): 104-11.
- [15] Hach, J. P. 1968. A very sensitive airborne microwave radiometer using two reference temperatures. *IEEE Transactions on Microwave Theory and Techniques* MTT-16 (9): 629-36.
- [16] Lagerloef, G. 1999. *Report on SSIWG Meeting 2*. Available: [http://www.esr.org/ssiwg-2/ssiwg\\_2.html](http://www.esr.org/ssiwg-2/ssiwg_2.html).
- [17] Ulaby, F. T., R. K. Moore, and A. K. Fung. 1981. *Microwave remote sensing active and passive Vol I, microwave remote sensing fundamentals and radiometry*, 456. Norwood, MA: Artech House.
- [18] Bendat, J. S., and A. G. Piersol. 1986. *Random data analysis and measurement procedures*. 2d ed. New York: John Wiley.
- [19] Skou, N. 1989. *Microwave radiometer systems: Design & analysis*, 162. Norwood, MA: Artech House.
- [20] Hardy, W. N., K. W. Gray, and A. W. Love. 1974. An S-band radiometer design with high absolute precision. *IEEE Trans. Micro. Theory and Tech* MTT-22:382-90.
- [21] Skolnik, M. I. 1980. *Introduction to radar systems*. 2d ed. New York: McGraw-Hill Book.
- [22] Dicke, R. H. 1946. The measurement of thermal radiation at microwave frequencies. *Review of Scientific Instruments* 17 (7): 268-74.
- [23] Hwei, P. H. 1970. *Fourier analysis*. New York: Simon and Schuster.

**Derek M. Burrage** completed his Ph.D. in oceanography at the University of Delaware in 1985. He then joined the Australian Institute of Marine Science where he combined physical oceanography with infra-red and microwave satellite remote sensing techniques to study circulation in the coastal ocean and marginal seas. During 1997-2000, he collaborated with Mal Heron and Mark Goodberlet to bring passive microwave surface salinity mapping technology to Australia, where they used it to map river plumes in the Great Barrier Reef Lagoon. In his present post with the University of Southern Mississippi, Department of Marine Science at Stennis Space Center, he works closely with the U.S. Naval Research Lab to further evolve this technology. His current research interests include river plume dynamics, systems simulation of air and space-borne radiometers, and hydro-dynamic modeling of surface and internal waves and currents. He is a long-serving member of the NASA/CNES and ESA international science teams for the TOPEX/JASON and ERS/ENVISAT radar satellite missions.

**Mark A. Goodberlet** received a mathematics B.S. degree from the University of Maine at Orono in 1977 and a Ph.D. in electrical engineering from the University of Massachusetts at Amherst in 1990. He has worked as a university instructor in electrical engineering and as a missile maintenance officer in the U.S. Army. For the past 12 years, he has been a senior microwave systems engineer at ProSensing (formerly Quadrant Engineering) in Amherst, Massachusetts, and has worked on the development of a variety of microwave remote sensing devices for meteorological and oceanographic applications. His present interests encompass passive microwave radiometer design, construction, and calibration.

**Malcolm L. Heron** received his undergraduate education from the University of Auckland, New Zealand in physics, and his Ph.D. in radio science from the same University in 1971. Since 1971, he has been with James Cook University in North Queensland, Australia where he is presently Professor of Physics. He has published over 100 refereed papers. His research interests are radio wave propagation, development of techniques for remote sensing of the environment, coastal oceanography, and meso-scale meteorology. He is presently the Chair of the North Queensland Section of IEEE and has been a member since 1977.